American Mineralogist, Volume 94, pages 557–564, 2009

Lattice compression and structural behavior of $NaVSi_2O_6$ clinopyroxene to 11 GPa

ANGELA ULLRICH,[1,*] RONALD MILETICH,[1] FABRIZIO NESTOLA,[2,3] CHRISTIAN WEIKUSAT[1] AND HARUO OHASHI[4]

[1]Institute of Geosciences, University of Heidelberg, Im Neuenheimer Feld 236, D-69120 Heidelberg, Germany
[2]Dipartimento di Geoscienze, Università di Padova, Via Giotto 1, I-10137 Padova, Italy
[3]CNR, IGG Unità di Padova, I-35137 Padova, Italy
[4]HASHI Institute for Silicate Science, Nishinakanobu 1-9-25, Shinagawa, Tokyo 142-0054, Japan

ABSTRACT

High-pressure behavior of a synthetic single crystal of the *C*2/*c* clinopyroxene $NaVSi_2O_6$ was investigated using X-ray diffraction and Raman spectroscopy in combination with diamond-anvil cell techniques. Lattice-parameters, single-crystal intensity data, and Raman spectra were collected up to pressures of about 11 GPa, revealing no discontinuity in the evolution of the lattice with increasing pressure. The fit of a third-order Birch-Murnaghan equation of state to the pressure-volume data yields a bulk modulus of $K_0 = 114.7$ (1.8) GPa with its pressure derivative $K' = 5.4$ (4). Strain analysis reveals compressional anisotropy with unit strain axial ratios of 1:2.9:3.1. The direction of largest compression was found to be perpendicular to the $(\bar{3}02)$ plane, which matches closely the direction of largest interlayer spacing between oxygen monolayers forming the structure of clinopyroxenes. The relatively large pressure dependency of the bulk modulus, compared to that of isostructural transition-metal compounds, was related to an increase in stiffness of the M2 polyhedron occurring above 4.6 GPa.

Keywords: Clinopyroxene, compressibility, high pressure, single crystal, X-ray diffraction

INTRODUCTION

Because pyroxenes are important phases of the Earth's crust and upper mantle, the systematics of their structural behavior under varying pressure, temperature, and/or chemical substitution has been subject of various studies (Yang and Prewitt 2000; Thompson and Downs 2004; Thompson et al. 2005). An important issue is the influence of incorporation of transition metal cations such as Fe^{3+}, Ti^{3+}, Cr^{3+}, and V^{3+} as well as divalent cations (Arlt et al. 1998; Ross and Reynard 1999; Ross and Sowerby 1999; Redhammer et al. 2003).

Common characteristics of all clinopyroxenes (cpx) are the chains of corner-sharing tetrahedra running parallel the crystallographic *c* axis, and these Si_2O_6 chains are linked laterally via bonding through the M1 and M2 cation sites. Hence the structural stability is determined mainly by the sizes of the M1 and M2 cations, and also the energy contributions from the *d*-electron configuration, i.e., the influence of crystal-field stabilization energy, which has been shown to be one important parameter that determines the structural stability of cpx (e.g., Arlt et al. 1998). Comparative high-pressure investigations on various $CaM^{2+}Si_2O_6$ and $NaM^{3+}Si_2O_6$ cpx, with and without incorporation of transition-metal cations, excluded a simple linear inverse relationship between bulk modulus, *K*, and unit-cell volume, as has been found for many isostructural series (Hazen et al. 2000 and references therein). The compression behavior of clinopyroxenes depends to a great extent on the pressure derivative of the bulk modulus $-dK/dP$, or K', which deviates in many cases significantly from 4. Whereas the bulk modulus seems to depend on the M1 site, K' seems to be mainly controlled by the size of the cation on the M2 site (Nestola et al. 2006). In addition a higher stiffness has been found in cpx with transition metal elements than without these elements (Origlieri et al. 2003; Zhang et al. 1997; Nestola et al. 2005) evidencing that not only the size of the M1 cation determines the bulk modulus, but also the valence electron character plays an important role for the compression behavior of cpx.

The subject of this study is the transition-metal compound $NaVSi_2O_6$, which is the end-member composition with trivalent vanadium on the M1 site. The crystal structure of the *C*2/*c* cpx was first determined by Ohashi et al. (1994), followed by several studies on $(Na,Ca)(V,Mg)Si_2O_6$ and $(Na,Ca)(V,Mn)Si_2O_6$ solid solutions (Ohashi et al. 2003a, 2003b) investigating the electronegativity and the 3*d*-electron distribution. It has been found that because of electron-electron repulsion between the *d*-electrons and the surrounding O atoms the V^{3+}-ion occupies a small distorted M1 site in the $(Na,Ca)(V,Mg)Si_2O_6$ system, whereas it can occupy a larger and less distorted site in $(Na,Ca)(V,Mn)Si_2O_6$. Recent studies on $NaVSi_2O_6$ and other quasi-one-dimensional vanadium-based (S = 1) chain compounds with pyroxene structure have been focused on the low-temperature behavior revealing the formation of a long-range three-dimensional Néel order (Vasiliev et al. 2004; Popović et al. 2006; Pedrini et al. 2007). Hence the question arises whether an analogous transition occurs with increasing pressure.

The present study aims to complement the low-pressure structural data on the end-member $NaVSi_2O_6$ with comparable investigations at high pressure. Apart from the measurements of structural changes for comparative crystal chemistry, high-precision data on lattice compression has been collected in order do determine EOS parameters and the unit-strain ellipsoid. A comparison of the recent data to isostructural *C*2/*c* cpx completes the investigation.

* E-mail: aullrich@min.uni-heidelberg.de

EXPERIMENTAL METHODS

Sample material and high-pressure conditions

Sample crystals are the same as those used in Ohashi et al. (1994). The crystals were synthesized by a solid-state reaction from a stoichiometric mixture of powder $Na_2Si_2O_5$, V_2O_3, and SiO_2 sealed in a platinum capsule. A belt-type high-pressure apparatus was used to maintain the capsule for 20 h at pressures of 6 GPa and temperatures of 1773 K. All of the crystals are of light green color and crystals of about 150 × 70 × 30 μm in size were chosen for the measurements in diamond-anvil cells (DACs).

All high-pressure investigations were carried out in opposed-anvil DACs, equipped with X-ray transparent beryllium-disk backing plates and a 12° optical port suitable for the spectroscopy applications. Sample crystal was loaded in an ETH-type DAC with standard geometry (height 1.4 mm, table 2.8 mm, girdle 3.0 mm) and culets of 600 μm diameters. Stainless steel gaskets provided the sample chamber of 200–250 μm in diameter with a thickness of about 90 μm. A 4:1 methanol:ethanol mixture was used as pressure-transmitting medium to achieve hydrostatic pressure conditions up to ~11 GPa. Since X-ray and Raman measurements were carried out on the same DAC loading, a quartz crystal and a ruby sphere were used as internal pressure markers.

Single-crystal X-ray diffraction

Lattice-parameter measurements at room pressure and 10 high pressures up to 10.70 GPa have been carried out on a Huber four-circle diffractometer using unmonochromatized Mo-radiation. Constrained lattice parameters of $NaVSi_2O_6$ and of the quartz crystal have been refined at each pressure from the positions of 20 Bragg reflections determined by the method of eight-position diffracted-beam centering (King and Finger 1979). By peak profile fitting the lattice parameters were refined with constraint to monoclinic and hexagonal, respectively, using the program SINGLE04 (Ralph and Finger 1982; Angel et al. 2000a). The pressure was monitored from the refined unit-cell volume of quartz, using the equation of state of quartz (Angel et al. 1997). Full intensity data sets were collected on a STOE STADI4 four-circle diffractometer (monochromatized Mo$K\alpha$ radiation), equipped with an Oxford Diffraction CCD detector, to $2\theta_{max} = 60°$ using an exposure time of 40 s and an ω-scan of 0.2°. The sample-to-detector distance was 60 mm. The CrysAlis RED program (Oxford Diffraction) was used to integrate the intensity data, applying a Lorentz-polarization correction. The absorption correction for the crystal, DAC, and gasket shadowing was performed using the program Absorb 6.0 (Angel 2004). Weighted isotropic structure refinements were done using the SHELX-97 package (Sheldrick 1997), starting from the atomic coordinates of $NaAlSi_2O_6$ cpx (Nestola et al. 2008) with space group *C*2/*c*, since no violation of the space group symmetry was detected. Experimental details are given in Table 1.

Raman spectroscopy

Raman spectra between 100 and 1100 cm^{-1} were obtained at five pressures between 1.7 and 9.1 GPa using a LabRam HR800UV spectrometer equipped with an OLYMPUS BXFM-ILHS optical microscope, automated x-y stage, a grating with 1800 grooves per millimeter, a Peltier-cooled CCD detector, and a 100× objective (numerical aperture 0.90). The 632.8 nm line of a He-Ne laser was used as the excitation source. The spectra were recorded in backscattered geometry with a lateral resolution of <1.5 μm, the wavenumber accuracy was 0.5 cm^{-1}, and the spectral resolution was 1 cm^{-1}. Pressures were determined by the ruby fluorescence method (Miletich et al. 2000 and references therein) using the He-Ne laser of the Raman spectrometer. The error in the observed pressure is estimated to be about 0.05 GPa.

RESULTS

Equations of state and strain analysis

Unit-cell data at ambient and high pressures determined in this study and the zero-pressure lattice-parameters determined by Ohashi et al. (1994) are given in Table 2. Although our crystal derives from the same sample material, there are small differences in lattice-parameter values, within about 5 to 6 times the e.s.d. values, that may be explained either from aberrations of the different instruments or material changes occurring during storage over 13 years. Figure 1a displays the change of the unit-cell volume with pressure. Within the e.s.d. values, the data sets

TABLE 2. Unit-cell parameters of $NaVSi_2O_6$ as a function of pressure

P (GPa)	V_{Qtz} (Å^3)	*a* (Å)	*b* (Å)	*c* (Å)	β (°)	*V* (Å^3)
0.0001*	112.994(10)	9.6339(4)*	8.7413(2)*	5.2960(3)*	106.905(2)*	426.72(3)*
0.0001	109.268(8)	9.6385(8)	8.7443(7)	5.2976(8)	106.915(9)	427.17(8)
1.376(3)	107.079(8)	9.6019(3)	8.7073(5)	5.2764(3)	106.747(4)	422.43(4)
2.343(4)	106.052(6)	9.5777(4)	8.6823(6)	5.2616(4)	106.634(4)	419.22(4)
2.844(3)	101.211(7)	9.5645(3)	8.6689(4)	5.2545(3)	106.578(3)	417.55(3)
5.674(5)	102.200(6)	9.5037(4)	8.5983(5)	5.2138(4)	106.231(4)	409.07(4)
5.026(4)	102.479(7)	9.5155(5)	8.6119(7)	5.2223(4)	106.307(4)	410.73(4)
4.850(4)	98.535(5)	9.5206(5)	8.6154(7)	5.2245(4)	106.331(4)	411.25(4)
7.636(4)	95.077(8)	9.4685(5)	8.5499(7)	5.1879(5)	106.016(5)	403.68(5)
10.696(8)	96.294(19)	9.431(3)	8.469(4)	5.1492(14)	105.663(18)	396.01(14)
9.544(17)	97.151(8)	9.446(3)	8.500(4)	5.1637(14)	105.812(17)	398.89(16)
8.783(7)		9.4477(7)	8.5243(3)	5.1732(3)	105.882(5)	400.72(4)

* Data collected by Ohashi et al. (1994).

TABLE 1. Experimental details of the intensity-data collection and the structure refinement of $NaVSi_2O_6$

Pressure (GPa)	0.0001	1.52	3.47	7.18	9.39	10.93	7.62	4.61	6.10
a (Å)	9.644(6)	9.614(8)	9.566(9)	9.496(10)	9.469(9)	9.453(9)	9.483(9)	9.545(8)	9.519(8)
b (Å)	8.749(6)	8.706(8)	8.659(8)	8.568(9)	8.521(8)	8.490(8)	8.565(8)	8.634(7)	8.598(7)
c (Å)	5.304(2)	5.278(4)	5.252(4)	5.201(4)	5.169(5)	5.150(5)	5.193(5)	5.233(4)	5.208(5)
β (°)	106.96(5)	106.86(5)	106.82(8)	106.25(8)	105.99(8)	105.89(8)	106.13(11)	106.59(9)	106.31(11)
V (Å^3)	428.06 4	422.78 4	416.42 4	406.26 4	400.93 4	397.52 4	405.18 4	413.31 4	409.09 4
Z	4	4	4	4	4	4	4	4	4
No. measured reflections	244	247	237	235	225	224	228	231	228
Unique reflections ($\|F_o\| > 4\theta$)	198	177	174	171	168	163	163	171	161
R_{int}	0.0271	0.0637	0.0524	0.0514	0.0487	0.0462	0.0458	0.0541	0.0529
Max. 2θ(°)	58.35	58.68	58.74	59.24	58.86	59.09	58.58	59.29	59.66
Range of *hkl*	$-10 < h < 9$	$-10 < h < 9$	$-10 < h < 9$	$-10 < h < 9$	$-10 < h < 9$	$-10 < h < 9$	$-10 < h < 9$	$-10 < h < 9$	$-10 < h < 9$
	$0 < k < 9$	$0 < k < 9$	$0 < k < 9$	$0 < k < 9$	$0 < k < 9$	$0 < k < 9$	$0 < k < 9$	$0 < k < 9$	$0 < k < 9$
	$0 < l < 7$	$0 < l < 7$	$0 < l < 7$	$0 < l < 7$	$0 < l < 7$	$0 < l < 7$	$0 < l < 7$	$0 < l < 7$	$0 < l < 7$
					Refinement				
$R1(\|F_o\| > 4\sigma)$	0.0428	0.0465	0.0459	0.0437	0.0443	0.0439	0.0427	0.0421	0.0433
*wR*2	0.0983	0.1257	0.1308	0.1074	0.0971	0.1100	0.0970	0.0970	0.1092
GooF	1.107	1.017	1.052	1.038	1.025	1.066	1.020	1.089	1.069
Parameters refined	30	22	22	22	22	22	22	22	22

Note: Data listed in order of collection, reliability factors have been determined according to: $R_{int} = \Sigma|F_o^2 - F_o^2(\text{mean})|/\Sigma[F_o^2]$, $R1 = \Sigma||F_o| - |F_c||/\Sigma|F_o|$, $wR2 = \{\Sigma[w(F_o^2 - F_c^2)^2]/\Sigma[w(F_o^2)^2]\}^{1/2}$, and GooF = $\{\Sigma[w(F_o^2 - F_c^2)^2]/(n - p)\}^{1/2}$, where n = number of reflections and p = total number of parameters refined.

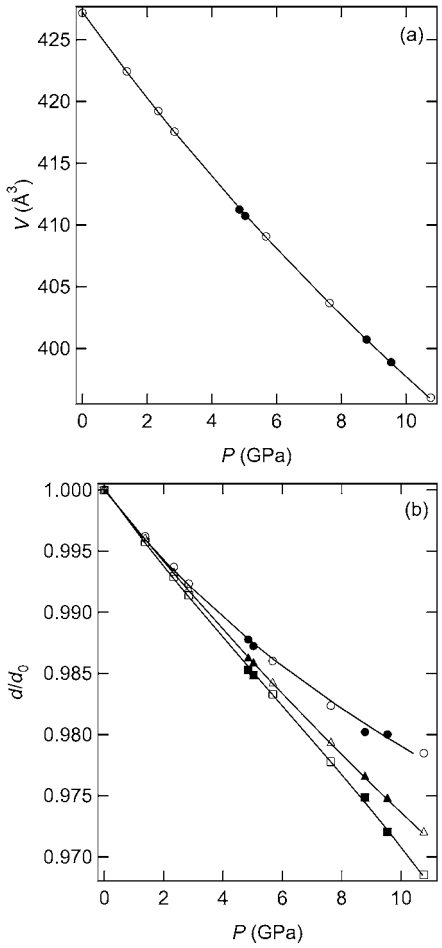

FIGURE 1. Compression behavior of the unit cell (open symbols show the data collected during compression, solid symbols the data collected during decompression, e.s.d. values are smaller than symbols). (**a**) Change of the unit-cell volume with pressure (the solid line represents the fit of a third-order Birch Murnaghan EOS to the measured data using the EOS parameters given in the text). (**b**) Change of the lattice parameters with pressure (a/a_0, b/b_0, and c/c_0 are represented by circles, squares, and triangles, respectively).

collected during compression and decompression are consistent and no discontinuity is apparent, suggesting continuous compression behavior. The fit of a single third-order Birch-Murnaghan equation of state (EOS; EOSFIT, Angel et al. 2000b) to the data set weighted according to the experimental uncertainties yields the parameters V_0 = 427.35 (10) Å^3, K_0 = 114.7 (1.8) GPa, and K' = 5.4 (4).

Regarding the compressibilities of the individual unit-cell axes (Fig. 1b), fits of linearized third-order Birch-Murnaghan EOS to their variations with pressure reveal compressional anisotropy [a_0 = 9.6408 (18) Å, K_0 = 105 (5) GPa with K' = 11.5 (1.6), b_0 = 8.7448 (11) Å, K_0 = 105 (2) GPa with K' = 2.3 (4) and c_0 = 5.2985 (5) Å, K_0 = 107.6 (1.6) GPa with K' = 3.6 (3)]. In particular, the EOS parameters obtained for the crystallographic *a* axis show large errors indicating an inappropriate use of the EOS-formulation to describe the significant curvature in the pressure-dependent variation of the *a* axis. The STRAIN software by Ohashi (Hazen and Finger 1982) has been used to determine the major deformation directions. A unit-strain ellipsoid calculated for the compression between 1 bar and 9.54 GPa reveals ratios of 1:2.9:3.1 for the principle axes, with the most compressible direction at an angle of 28.98° from the crystallographic *c* axis (according to the conventionally symmetry-constrained orientation of the strain ellipsoid).

Structure refinement

The results of structure refinements on the single-crystal intensity data are summarized in Tables 3 and 4. The zero-pressure lattice-parameters differ slightly from the ones determined during the lattice-parameter data collection, which could be due to the use of different sample crystals, although the zero-pressure structure determined in this study is consistent with the one described by Ohashi et al. (1994). According to the site symmetry 2 of the M1 and M2 sites (position 4*e*), there are three pairs of symmetrically equivalent M-O distances in both the M1 octahedron and the M2 polyhedron. Depending on whether two additional M2-O3 bonds (2.81 Å at 1 bar) are considered, the coordination of the M2 cation is described as 6 or 6+2 fold. The M2 site, which corresponds to the equivalent site of eightfold-coordinated M2 in other silicate cpx, can be considered highly distorted to accommodate these additional bonds (Fig. 2).

For the $NaVSi_2O_6$ cpx at ambient pressure three pairs of M2-O distances between 2.39 and 2.42 Å and two M2-O bonds at a distance of 2.81 Å (Na-O3c2/d2) suggest a distorted octahedral coordination, which is also supported by bond-valence arguments. The individual M2-O bond lengths decrease continuously with the largest shortening rate observed in M2-O2c2/d2 (Fig. 3a) resulting in a slight increase in BLD from 0.4(2) to 1.3(3)%. The M2-O3c2/d2 bonds, which determine the coordination change from 6 to 6+2, show a linear decrease without any obvious rate changes of bond-length compression.

The M1 site forms a more regular octahedron with three pairs of symmetrically equivalent bonds between 1.947 and 2.070 Å (Fig. 3b). The polyhedral distortion corresponds to a 2 + 4 distortion similar to a typically Jahn-Teller distorted uniaxially compressed octahedron, which is indicative of the distribution of the two *d* electrons in the non-bonding orbitals of the d^2-configuration of the V^{3+} cations (Ohashi et al. 2003b). Within the experimental errors, all of the bond lengths decrease almost linearly on compression. Accordingly, there is no significant change in BLD parameter observed, implying the continuous regularization of the $M1O_6$ octahedron on increasing pressure, as also expressed by other distortion parameters (Table 4). Almost insignificant changes can be observed for the polyhedral geometry of the SiO_4 group. By comparing the variations in polyhedral volumes (Fig. 3c), the largest compression is found for the M2 polyhedron, revealing a bulk modulus of 53(5) GPa compared to 184(13) and 333(44) GPa determined for the polyhedral compression of the M1 octahedron and the Si tetrahedron, respectively. Whereas all of the polyhedral volumes decrease continuously, the M2 polyhedron reveals an increase in stiffness above 4.6 GPa that coincides with the crossover of the M2-O1a1/b1 and the M2-O2c2/d2 bond lengths. However, as observed for the individual M-O bond lengths, the M1-M2 distance decreases continuously at a rate of 0.9% in the investigated pressure range (Fig. 3d).

TABLE 3. Pressure-dependent variation of atom positions and atomic displacement factors determined for $NaVSi_2O_6$

	Multiplicity Wykoff letter Site symmetry	Parameter	0.0001 GPa	1.52 GPa	3.47 GPa	7.18 GPa	9.39 GPa	10.93 GPa	7.62 GPa	4.61 GPa	6.10 GPa
Na	4*e* 2	*y*	0.3017(5)	0.3021(6)	0.3049(6)	0.3064(6)	0.3081(6)	0.3097(7)	0.3068(6)	0.3049(7)	0.3055(7)
		U	0.0147(16)	0.0165(12)	0.0151(13)	0.0134(11)	0.0134(11)	0.0121(12)	0.0145(11)	0.0158(11)	0.0142(12)
V	4*e* 2	*y*	0.9050(2)	0.9056(2)	0.9059(3)	0.9068(3)	0.9078(3)	0.9076(3)	0.9072(3)	0.9062(3)	0.9067(3)
		U	0.0062(6)	0.0078(6)	0.0072(7)	0.0074(6)	0.0062(6)	0.0059(6)	0.0069(6)	0.0069(6)	0.0061(6)
Si	8*f* 1	*x*	0.2913(2)	0.2918(3)	0.2921(3)	0.2922(3)	0.2921(3)	0.2920(3)	0.2921(3)	0.2918(3)	0.2920(3)
		y	0.0909(3)	0.0916(3)	0.0918(3)	0.0930(3)	0.0934(3)	0.0937(3)	0.0928(3)	0.0926(3)	0.0923(3)
		z	0.2390(3)	0.2393(4)	0.2397(5)	0.2401(4)	0.2399(4)	0.2400(4)	0.2399(4)	0.2398(4)	0.2400(4)
		U	0.0076(6)	0.0076(6)	0.0076(7)	0.0067(6)	0.0062(6)	0.0067(6)	0.0069(5)	0.0065(6)	0.0061(6)
O1	8*f* 1	*x*	0.1159(6)	0.1153(7)	0.1143(8)	0.1157(6)	0.1150(6)	0.1153(6)	0.1154(6)	0.1148(6)	0.1148(6)
		y	0.0790(6)	0.0802(6)	0.0823(7)	0.0831(7)	0.0845(7)	0.0844(7)	0.0829(7)	0.0809(7)	0.0817(7)
		z	0.1446(8)	0.1439(10)	0.1451(11)	0.1455(9)	0.1457(9)	0.1459(9)	0.1457(9)	0.1448(8)	0.1453(9)
		U	0.0080(10)	0.0066(12)	0.0076(13)	0.0061(12)	0.0055(11)	0.0043(12)	0.0062(11)	0.0045(11)	0.0052(12)
O2	8*f* 1	*x*	0.3605(7)	0.3602(8)	0.3605(9)	0.3596(8)	0.3601(8)	0.3605(8)	0.3615(7)	0.3613(7)	0.3610(8)
		y	0.2577(6)	0.2574(7)	0.2590)7)	0.2605(7)	0.2612(7)	0.2607(8)	0.2594(7)	0.2581(7)	0.2582(7)
		z	0.3058(9)	0.3098(11)	0.3123(12)	0.3183(11)	0.3220(11)	0.3238(11)	0.3200(10)	0.3153(10)	0.3170(11)
		U	0.0113(12)	0.0110(14)	0.0110(15)	0.0102(13)	0.0092(13)	0.0096(15)	0.0087(13)	0.0077(13)	0.0077(14)
O3	8*f* 1	*x*	0.3519(7)	0.3525(7)	0.3528(8)	0.3553(7)	0.3550(7)	0.3563(8)	0.3558(8)	0.3543(8)	0.3550(8)
		y	0.0090(6)	0.0113(7)	0.0133(8)	0.0168(7)	0.0188(7)	0.0193(8)	0.0176(7)	0.0137(7)	0.0155(7)
		z	0.0135(9)	0.0101(10)	0.0091(12)	0.0044(10)	0.0021(10)	0.0005(11)	0.0037(10)	0.0076(10)	0.0047(10)
		U	0.0097(11)	0.089(12)	0.0101(14)	0.0090(12)	0.0083(12)	0.0082(12)	0.0095(11)	0.0098(12)	0.0086(12)

TABLE 4. Selected bond lengths (Å), polyhedral volumes ($Å^3$), angles (°), and distortion parameters (Renner and Lehmann 1986) determined at different pressures

	0.000 GPa	1.52 GPa	3.47 GPa	7.18 GPa	9.39 GPa	10.93 GPa	7.62 GPa	4.61 GPa	6.1 GPa
M2 (Na)									
M2-O1a1,b1	2.392(6)	2.373(7)	2.359(8)	2.344(7)	2.320(7)	2.336(8)	2.345(7)	2.346(6)	2.351(8)
M2-O2c2,d2	2.405(6)	2.379(7)	2.366(7)	2.339(7)	2.330(7)	2.309(7)	2.324(7)	2.364(7)	2.337(7)
M2-O3c1,d1	2.420(6)	2.427(7)	2.410(8)	2.406(7)	2.405(8)	2.389(8)	2.407(8)	2.405(8)	2.410(8)
M2-O3c2,d2	2.811(6)	2.769(6)	2.724(7)	2.637(6)	2.598(6)	2.565(7)	2.621(6)	2.697(7)	2.658(7)
$<M2\text{-}O>_6$	2.406(3)	2.393(4)	2.388(5)	2.373(4)	2.352(4)	2.344(4)	2.359(4)	2.372(4)	2.366(4)
$V(M2)_6$	12.15(4)	11.71(5)	11.37(5)	10.86(5)	10.65(5)	10.55(5)	10.78(5)	10.98(5)	10.87(5)
BLD $(\%)_6$	0.4(2)	0.9(2)	1.0(3)	1.3(2)	1.5(2)	1.3(3)	1.4(3)	0.9(2)	1.2(3)
$<M2\text{-}O>_8$	2.507(3)	2.487(3)	2.500(4)	2.432(3)	2.413(3)	2.400(4)	2.424(4)	2.453(3)	2.439(4)
$V(M2)_8$	26.05(11)	25.49(13)	24.91(14)	24.02(12)	23.54(12)	23.16(13)	23.76(12)	24.52(13)	24.14(13)
BLD $(\%)_8$	6.07(17)	5.67(19)	5.9(2)	4.7(2)	3.8(2)	3.4(2)	4.1(2)	5.0(2)	4.5(2)
M1 (V)									
M1-O2c1,d1	1.947(6)	1.954(7)	1.939(7)	1.934(6)	1.930(6)	1.927(6)	1.930(6)	1.940(6)	1.939(6)
M1-O1a2b2	2.060(5)	2.052(6)	2.045(7)	2.029(6)	2.017(6)	2.012(6)	2.021(6)	2.031(6)	2.023(6)
M1-O1a1b1	2.070(5)	2.057(6)	2.049(6)	2.045(5)	2.036(5)	2.033(6)	2.044(5)	2.047(5)	2.044(6)
<M1-O>	2.026(3)	2.021(3)	2.011(4)	2.003(3)	1.994(3)	1.991(3)	1.998(3)	2.006(3)	2.002(3)
<M1-O1>	2.065(3)	2.054(4)	2.047(5)	2.037(4)	2.026(4)	2.022(4)	2.033(4)	2.039(4)	2.034(4)
V_{M1}	10.96(2)	10.88(5)	10.72(5)	10.59(4)	10.46(4)	10.41(5)	10.54(4)	10.64(4)	10.59(5)
BLD (%)	2.6(2)	2.2(2)	2.4(3)	2.3(2)	2.2(3)	2.1(3)	2.3(2)	2.2(2)	2.1(2)
OAV $(°)^2$	26.1(7)	25.2(9)	25.9(1.0)	23.8(9)	23.3(9)	22.4(9)	21.5(8)	23.9(8)	22.9(9)
<O-O>	2.861(2)	2.855(2)	2.840(2)	2.829(2)	2.817(2)	2.812(2)	2.823(2)	2.833(2)	2.828(2)
ELD (%)	2.98(10)	2.93(11)	2.89(12)	2.89(11)	2.82(11)	2.81(11)	2.75(10)	2.93(11)	2.89(11)
$<O\text{-}O>_{shared}$	2.817(3)	2.800(4)	2.776(4)	2.773(4)	2.756(4)	2.753(4)	2.764(3)	2.771(4)	2.768(4)
$<O\text{-}O>_{unshared}$	2.893(3)	2.893(3)	2.886(3)	2.868(3)	2.861(3)	2.855(3)	2.865(3)	2.877(3)	2.871(3)
e_u/e_s	1.0272(14)	1.0332(17)	1.0397(19)	1.0342(17)	1.0381(17)	1.0371(18)	1.0365(15)	1.0380(16)	1.0374(17)
Si									
Si-O2	1.601(6)	1.585(6)	1.589(7)	1.578(7)	1.578(7)	1.569(7)	1.578(6)	1.578(7)	1.575(7)
Si-O1	1.622(6)	1.627(7)	1.630(8)	1.612(7)	1.615(6)	1.609(7)	1.612(6)	1.623(6)	1.621(7)
Si-O3	1.641(5)	1.644(6)	1.635(7)	1.635(6)	1.631(6)	1.626(7)	1.636(6)	1.638(6)	1.630(7)
Si-O3	1.652(5)	1.644(6)	1.640(7)	1.642(5)	1.635(5)	1.643(6)	1.642(5)	1.646(5)	1.646(6)
<Si-O>	1.629(3)	1.625(3)	1.624(4)	1.617(3)	1.615(3)	1.612(3)	1.617(3)	1.621(3)	1.618(3)
$d_{br\text{-}nbr}$	0.035(5)	0.038(6)	0.028(7)	0.043(6)	0.037(6)	0.046(7)	0.044(6)	0.041(6)	0.040(7)
$V_{tetrahedron}$	2.205(7)	2.190(8)	2.187(9)	2.159(8)	2.150(8)	2.136(8)	2.158(8)	2.174(8)	2.161(9)
BLD (%)	1.1(3)	1.2(3)	1.1(3)	1.3(3)	1.1(3)	1.4(3)	1.4(3)	1.3(3)	1.3(3)
TAV $(°)^2$	16.5(1.0)	15.8(1.2)	12.6(1.2)	13.4(1.0)	13.5(1.0)	16.1(1.2)	16.2(1.1)	17.9(1.2)	16.2(1.2)
O1-Si-O2	117.2(3)	116.9(3)	116.1(4)	116.0(3)	115.9(3)	116.3(4)	116.8(3)	117.3(3)	116.9(3)
Si-O3-Si	139.8(3)	139.5(5)	139.2(5)	137.1(5)	136.7(5)	135.6(5)	136.5(5)	138.0(5)	137.2(5)
O3-O3-O3	173.2(4)	171.5(5)	170.0(6)	167.4(5)	165.9(5)	165.5(6)	166.8(5)	169.7(5)	168.3(5)
M1-O1-M1	98.5(2)	98.3(3)	98.0(3)	97.0(2)	96.6(2)	96.4(3)	97.0(2)	98.0(2)	97.5(3)
M1-M2	3.210(3)	3.199(4)	3.198(4)	3.178(4)	3.172(4)	3.168(4)	3.178(4)	3.189(4)	3.180(4)
M1-M1	3.130(3)	3.109(3)	3.091(3)	3.052(3)	3.025(3)	3.015(3)	3.044(3)	3.077(3)	3.059(3)

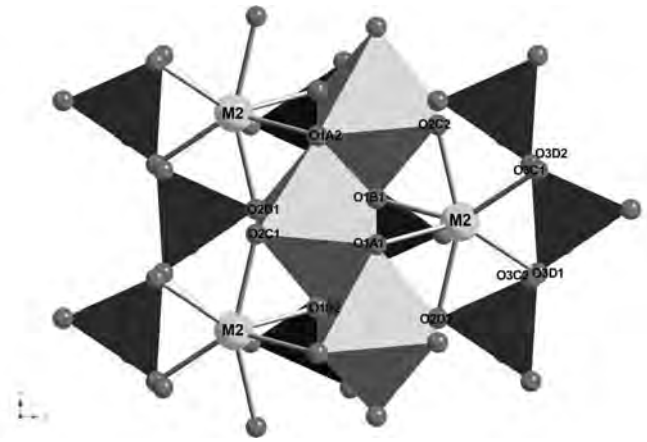

FIGURE 2. The structure of $NaVSi_2O_6$ viewed down the crystallographic *a*-axis. The SiO_4-tetrahedra and the VO_6-octahedra are shown as polyhedra. The O atoms are labeled after Burnham et al. (1967).

The geometric mismatch occurring between the M2-polyhedra and the M1-octahedra due to different compressibilities is accommodated by the kinking of the SiO_4 chain (Fig. 4a). The O3-O3-O3 angle is O-rotated, and decreases by 4%. The observed increase in tetrahedral chain kinking is accompanied by a rotation of the SiO_4 tetrahedra around the normal to the tetrahedral basal plane, which is expressed by a 3% decrease in the Si-O3-Si angle (Fig. 4b). The O2 atoms interconnect the chains of tetrahedra and the chains of octahedra along *b*, and the O1 atoms connect the tetrahedra with the M1 octahedra along *a*. The increase in kinking and also in the tilt angle of the Si-O chains can be associated with a large decrease in O-O distances shared with the M2 polyhedra.

Raman spectra

Selected Raman spectra are depicted in Figure 5, revealing continuous change during the process of loading pressure. The bands have been assigned according to the spectra of structurally

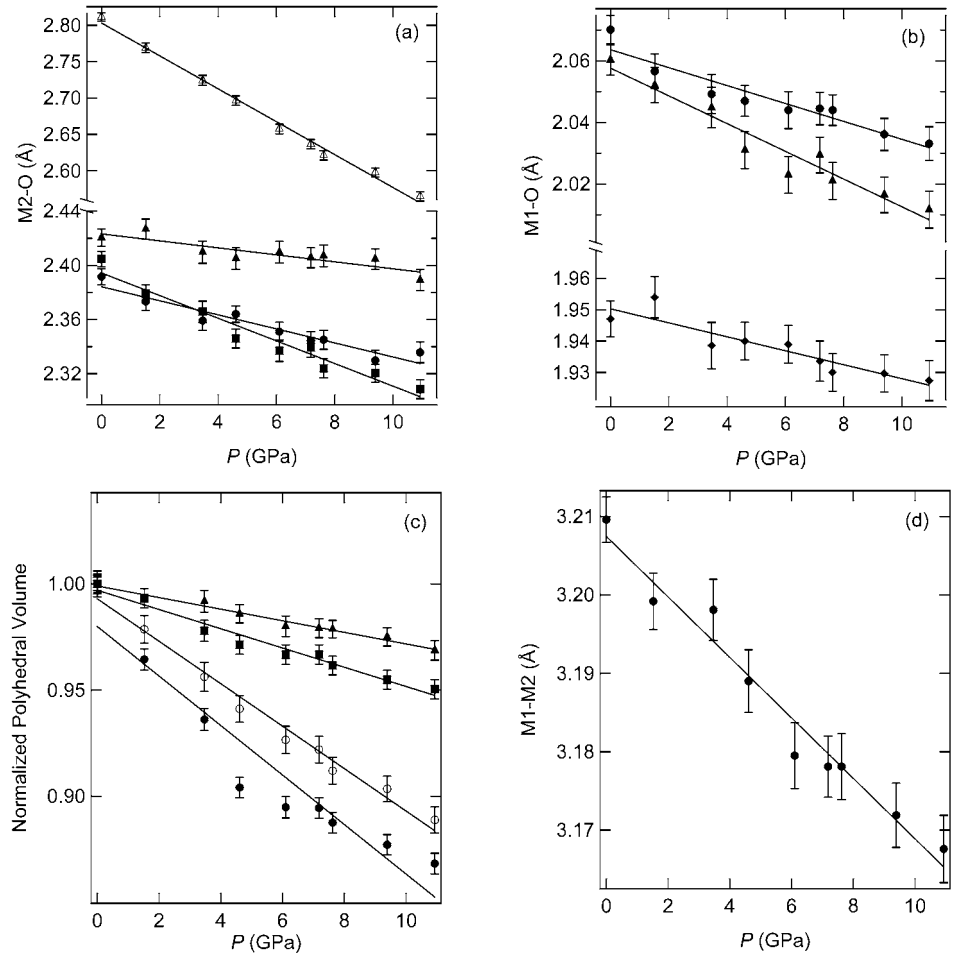

FIGURE 3. Variation in bond lengths, polyhedral volumes, and M1-M2 distances with pressure: lines represent linear fits to the data. (**a**) Pressure-dependent change of the individual Na-O bond lengths (M2-O1a1/b1 bonds are represented by circles, M2-O2c2/d2 by squares, M2-O3c1/d1 by solid triangles, and M2-O3c2/d2 by open triangles). (**b**) Variation of V-O distances (M1-O1a1/b1, M1-O1a2b2, and M1-O2c1/d1 bond lengths are shown by circles, squares, and triangles). (**c**) Normalized polyhedral volumes of NaO_6 (closed circles), NaO_8 (open circles), VO_6 (squares), and SiO_4 (triangles). Bulk moduli determined from linear fits to the measured data are given in the text. (**d**) Interatomic distance between M1 and M2 cations.

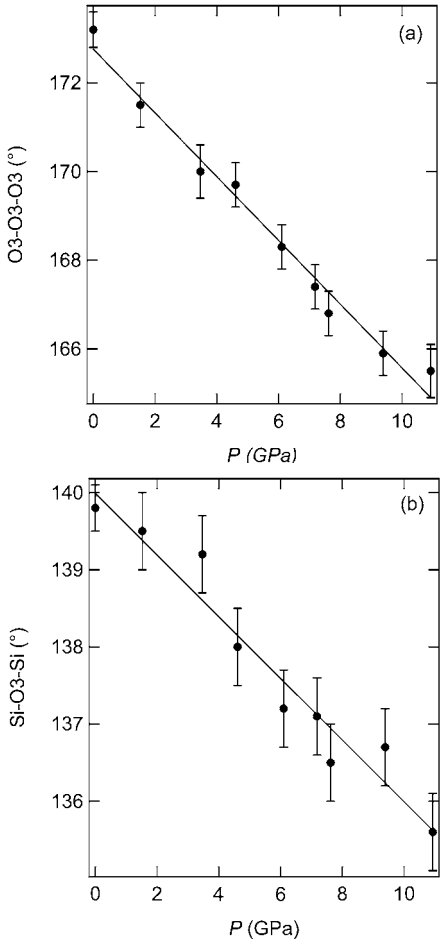

FIGURE 4. Changes in tetrahedral chain geometry with pressure. (**a**) Increase in tetrahedral chain kinking. (**b**) Rotation of the SiO_4 tetrahedra around the normal to the tetrahedral basal plane.

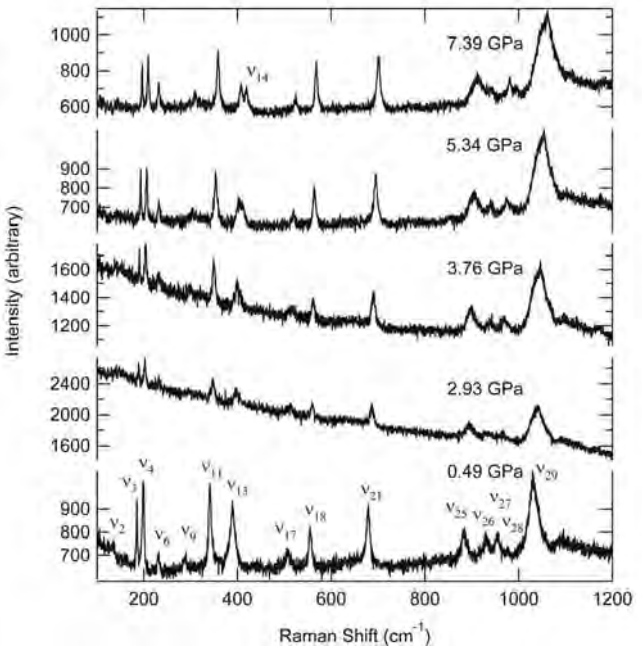

FIGURE 5. Selected Raman spectra of $NaVSi_2O_6$ varying with pressure; peaks have been labeled according to the isostructural $NaTiSi_2O_6$ cpx (Popović et al. 2005; Konstantinović et al 2004).

isomorphous $NaTiSi_2O_6$ (Popović et al. 2005; Konstantinović et al. 2004), where 29 of 30 phonon modes expected from factor-group analysis have been recorded. The spectra of $NaTiSi_2O_6$ and $NaVSi_2O_6$ agree to a large extent, although not all of the bands have been found in the latter. This can be ascribed mainly to strong background luminescence that creates a low signal-to-noise ratio and suppresses low intensity peaks. A significant increase in background, especially in the low-frequency region, is observed between 0.49 and 5.34 GPa, which indicates the occurrence of a pressure-induced structural disorder. In the low wavenumber region assigned to complex lattice vibrations due to Si-O bending and M-O interactions, peak υ_{13}, related to (O_1-V-O_1) bending vibrations, seems to split into υ_{13} and υ_{14} with increasing pressure. But considering that the FWHM of υ_{13} is 13.70 cm^{-1} at 0.49 GPa and that the peaks υ_{13} and υ_{14} are expected to be only 5.78 cm^{-1} apart at this pressure, it appears that υ_{13} consists of both peaks, separating with pressure. The wavenumber range between 900 and 1100 cm^{-1} attributed to Si-$O_{1,2}$ and V-$O_{1,2}$ stretching vibrations is dominated by the occurrence of very broad and overlapping peaks thus rendering impossible the unambiguous determination of peak positions. The high wavenumber phonon lines become even broader with increasing pressure, indicating an increase in bond fluctuations in the VO_6 octahedra, whereas no change has been observed in the region of Si-O_3 stretching vibrations between 600 and 900 cm^{-1}. At 11 pressures up to 9.9 GPa, band positions of selected vibrational modes have been obtained from fits of Lorentzian polynomials to the measured data, and their pressure dependent shifts are presented in Figure 6. Apart from the separation of υ_{13} into υ_{13} and υ_{14} all of the peaks shift continuously toward higher wavenumbers with pressure.

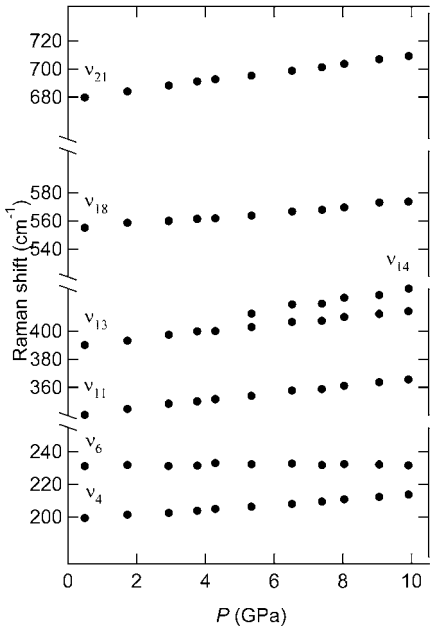

FIGURE 6. Continuous change of selected vibrational modes with pressure.

DISCUSSION

By comparing the results of this study with existing high-pressure data on cpx, it was found that the high-pressure behavior of $NaVSi_2O_6$ confirms previous observations on cpx compression in general to a large extend.

By analogy to studies in other cpx, the value determined for K' deviates significantly from 4 ($K' = 5.4$) confirming that the effect of K' has to be taken into account in the comparison of compressibilities of cpx. Hence the V/V_0 ratio has been calculated from the EOS of various cpx. A comparison of the compressibility of $NaVSi_2O_6$ to other transition-metal containing $NaM^{3+}Si_2O_6$ cpx, has shown a linear dependence between V/V_0 and the ionic radius of the M1 cation (Fig. 7), whereas the EOS determined for $NaAlSi_2O_6$ reveals, as expected, a larger compressibility.

Principle axes and the orientation of the unit-strain ellipsoid determined for $NaVSi_2O_6$ are similar to those calculated for diopside, hedenbergite (Zhang et al. 1997), aegirine (Downs et al. 2006), jadeite (Nestola et al. 2006), and kosmochlor (Origlieri et al. 2003). In all of these $C2/c$ pyroxenes the SiO_4 chain is O-rotated (O3-O3-O3 < 180°) and their compressional anisotropy can be understood by considering these cpx structures as based on cubic closest packing (ccp) of O atoms (Thompson and Downs 2003) with stacking directions perpendicular to (100), $(\bar{1}01)$, (131), and $(1\bar{3}1)$. Room-pressure $NaVSi_2O_6$ reveals an O3-O3-O3 angle of 173.2° at zero pressure, i.e., O-rotated SiO_4 chains show cubic closest packing of O atoms, and the distances between the oxygen monolayers have been determined to be 2.31, 2.56, 2.36, and 2.36 Å, respectively. Hence the highest compression that has been found perpendicular to the $(\bar{3}02)$ plane matches closely with the direction of largest interlayer spacing and approaches it as pressure is increased. Movement of the O atoms toward ideal ccp is indicated by the O3-O3-O3 angle decreasing with a slope of –0.72. This is consistent with the pressure-dependent kinking observed in the SiO_4 chains in kosmochlor, revealing a similar zero pressure O3-O3-O3 angle of 172.8 decreasing with a slope of –0.69. By comparing the zero pressure structure of $NaVSi_2O_6$ to the structure of kosmochlor, not only similar values for the SiO_4 kinking angle have been found, but also the zero pressure tilt angles of the SiO_4 chains are similar. The difference between the ionic radii of V^{3+} (0.64) and Cr^{3+} (0.615) results only in slight differences in the M1 and M2 polyhedral volumes [$V(NaO_6)$ = 11.826 Å^3 and $V(CrO_6)$ = 10.422 Å^3 in kosmochlor], hence also in the polyhedral compressibilities. Whereas the VO_6 octahedron (K_0 = 184 GPa) reveals a significantly larger stiffness than the CrO_6 octahedron (K_0 = 90 GPa), the bulk modulus of the NaO_6 polyhedron reveals larger compressibility for $NaVSi_2O_6$ (K_0 = 53 GPa, as opposed to 70 GPa for kosmochlor). A smaller overall bulk modulus has been found for $NaVSi_2O_6$, compared to K_0 = 134 GPa, which has been determined for kosmochlor. However in addition a significant pressure dependency has been found for the bulk modulus of $NaVSi_2O_6$ ($K' = 5.6$ compared to $K' = 2.0$ determined for kosmochlor). This can be ascribed to the compression behavior of the M2 polyhedron revealing an increase in stiffness above 4.6 GPa.

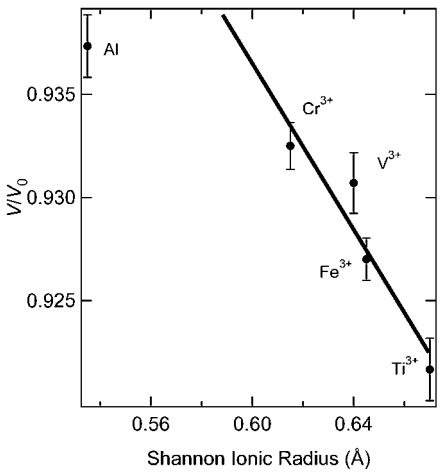

FIGURE 7. V/V_0 ratio at 10 GPa calculated from the Birch-Murnaghan EOS of various $NaM^{3+}Si_2O_6$ clinopyroxenes plotted vs. Shannon Ionic Radius of the M^{3+} cation: $NaVSi_2O_6$ (this study), $C2/c$-$NaTiSi_2O_6$ (Ullrich et al. 2008), kosmochlor (Origlieri et al. 2003), aegirine (Downs and Singh 2006), and jadeite (Nestola et al. 2006).

In conclusion, the cpx $NaVSi_2O_6$ has been found to fit approximately the compression trend observed for other transition-metal-containing cpx, and in addition it reveals a similar orientation of the unit-strain ellipsoid. However, due to an increase in stiffness of the main compressibility-determining structural unit (the M2 polyhedron), the bulk modulus shows a relatively large pressure dependency that has to be taken into account by comparing the compressibility of $NaVSi_2O_6$ to other cpx.

ACKNOWLEDGMENTS

This research was supported by the Deutsche Forschungsgemeinschaft (DFG) Grant no. MI 605/2-2. Special thanks are also due to the GSI, Gesellschaft für Schwerionenforschung mbH, Darmstadt (Materials Research Group) for providing the possibility to use the Raman spectrometer.

REFERENCES CITED

Angel, R.J. (2004) Absorption corrections for diamond-anvil cells implemented in the software package Absorb 6.0. Journal of Applied Crystallography, 37, 486–492.

Angel, R.J., Allan, D.R., Miletich, R., and Finger, L.W. (1997) The use of quartz as an internal pressure standard in high-pressure crystallography. Journal of Applied Crystallography, 30, 461–466.

Angel, R.J., Downs, R.T., and Finger, L.W. (2000a) High-temperature—high-pressure diffractometry. In R.M. Hazen and R.T. Downs, Eds., High-Temperature and High-Pressure Crystal Chemistry, 41, p. 559–596. Reviews in Mineralogy a nd Geochemistry, Mineralogical Society of America and Geochemical Society, Chantilly, Virginia.

——— (2000b) Equations of state. In R.M. Hazen and R.T. Downs, Eds., High-Temperature and High-Pressure Crystal Chemistry, 41, p. 35–60. Reviews in Mineralogy and Geochemistry, Mineralogical Society of America and Geochemical Society, Chantilly, Virginia.

Arlt, T., Angel, R.J., Miletich, R., Armbruster, T., and Peters, T. (1998) High-pressure $P2_1/c$-$C2/c$ phase transition in clinopyroxenes: Influence of cation size and electronic structure. American Mineralogist, 83, 1176–1181.

Burnham, C.W., Clark, J.R., Papike, J.J., and Prewitt, C.T. (1967) A proposed crystallographic nomenclature for clinopyroxene structures. Zeitschrift für Kristallographie, 125, 109–119.

Downs, R.T. and Singh, A.K. (2006) Analysis of deviatoric stress from nonhydrostatic pressure on a single crystal in a diamond anvil cell: The case of monoclinic aegirine, $NaFeSi_2O_6$. Journal of Physics and Chemistry of Solids, 67, 1995–2000.

Hazen, R.M. and Finger, L.W. (1982) Comparative Crystal Chemistry, 231 p. Wiley, New York.

Hazen, R.M., Downs, R.T., and Prewitt, C.T. (2000) Principles of comparative crystal chemistry. In R.M. Hazen and R.T. Downs, Eds., High-Temperature and High-Pressure Crystal Chemistry, 41, p. 1–34. Reviews in Mineralogy and Geochemistry, Mineralogical Society of America and Geochemical Society, Chantilly, Virginia.

King, H.E. and Finger, L.W. (1979) Diffracted beam crystal centering and its application to high-pressure crystallography. Journal of Applied Crystal-

lography, 12, 374–378.
Konstantinović, M.J., van den Brink, J., Popović, Z.V., Moshchalkov, V.V., Isobe, M., and Ueda, Y. (2004) Orbital dimerization in $NaTiSi_2O_6$: An orbital analogue of the spin-Peierls phase transition. Physical Review, B69, 020409.
Miletich, R., Allan, D.R., and Kuhs, W.F. (2000) High-pressure single-crystal techniques. In R.M. Hazen and R.T. Downs, Ed., High-Temperature and High-Pressure Crystal Chemistry, 41, p. 445–520. Reviews in Mineralogy and Geochemistry, Mineralogical Society of America and Geochemical Society, Chantilly, Virginia.
Nestola, F., Boffa-Ballaran, T., Tribaudino, M., and Ohashi, H. (2005) Compressional behaviour of $CaNiSi_2O_6$ clinopyroxenes: bulk modulus systematic and cation type in clinopyroxenes. Physics and Chemistry of Minerals, 32, 222–227.
Nestola, F., Boffa-Ballaran, T., Liebske, C., Bruno, M., and Tribaudino, M. (2006) High-pressure behavior along the jadeite $NaAlSi_2O_6$-aegirine $NaFeSi_2O_6$ solid solution up to 10 GPa. Physics and Chemistry of Minerals, 33, 417–425.
Nestola, F., Boffa-Ballaran, T., Liebske, C., Thompson, R., and Downs, R.T. (2008) The effect of the hedenbergitic substitution on the compressibility of jadeite. American Mineralogist, 93, 1005–1013.
Ohashi, H., Osawa, T., and Sato, A. (1994) $NaVSi_2O_6$. Acta Crystallographica, C50, 1652–1655.
——— (2003a) Crystal structures of $(Na,Ca)(V,Mn)Si_2O_6$ pyroxenes. In H. Ohashi, Ed., X-ray study on Si-O bonding, 59 p. Maruzen Publishing Service Center, Tokyo.
——— (2003b) Crystal structures of $(Na,Ca)(V,Mg)Si_2O_6$ pyroxenes. In H. Ohashi, Ed., X-ray Study on Si-O Bonding, 72 p. Maruzen Publishing Service Center, Tokyo.
Origlieri, M.J., Downs, R.T., Thompson, R.M., Pommier, C.J.S., Bonner Denton, M., and Harlow, G.E. (2003) High-pressure crystal structure of kosmochlor, $NaCrSi_2O_6$, and systematics of anisotropic compression in pyroxenes. American Mineralogist, 88, 1025–1032.
Pedrini, B., Gavilano, J.L., Ott, H.R., Kazakov, S.M., and Karpinski, J. (2007) Quenching of the Haladane gap in $LiVSi_2O_6$ and related compounds. The European Physical Journal B: Condensed Matter and Complex Systems, 55, 219–228.
Popović, Z.V., Konstantinović, M.J., Dohčević-Mitrović, Z., Isobe, M., and Ueda, Y. (2006) Orbital and lattice dynamics in pyroxenes. Physica B, 378, 1072–1074.
Popović, Z.V., Konstantinović, M.J., Popov, V.N., Cantarero, A., Dohčević-Mitrović, Z., Isobe, M., and Ueda, Y. (2005) Optical phonons in the $NaTiSi_2O_6$ oxide with S = ½ spin chains. Physical Review B, 71, 224302.
Ralph, R.L. and Finger, L.W. (1982) A computer program for refinement of crystal orientation matrix and lattice constants from diffractometer data with lattice symmetry constraints. Journal of Applied Crystallography, 15, 537–539.
Redhammer, G.J., Ohashi, H., and Roth, G. (2003) Single-crystal structure refinement of $NaTiSi_2O_6$ clinopyroxene at low temperatures ($298 < T < 100$ K). Acta Crystallographica B, 59, 730–746.
Renner, B. and Lehmann, G. (1986) Correlation of angular and bond length distortion in TO_4 units in crystals. Zeitschrift für Kristallographie, 175, 43–59.
Ross, N.L. and Reynard, B. (1999) The effect of iron on the $P2_1/c$ to $C2/c$ transition in $(Mg,Fe)SiO_3$ clinopyroxenes. European Journal of Mineralogy, 11, 585–589.
Ross, N.L. and Sowerby, J.R. (1999) High-pressure crystal-field spectra of single-crystal clinoferrosilite. European Journal of Mineralogy, 11, 791–801.
Sheldrick, G.M. (1997) SHELX, programs for Crystal Structure Analysis. University of Göttingen, Germany.
Thompson, R.M. and Downs, R.T. (2003) Model pyroxenes I: Ideal pyroxene topologies. American Mineralogist, 88, 653–666.
——— (2004) Model pyroxenes II: Structural variations as a function of tetrahedral rotation. American Mineralogist, 89, 614–628.
Thompson, R.M., Downs, R.T., and Redhammer, G.J. (2005) Model pyroxenes III: Volume of $C2/c$ pyroxenes at mantle P, T and x. American Mineralogist, 90, 1840–1851.
Vasiliev, A.N., Ignatchik, O.L., Isobe, M., and Ueda, Y. (2004) Long range Néel order in quasi-one-dimensional vanadium-based (S=1) pyroxenes (Li, Na) $V(Si, Ge)_2O_6$. Physical Review, B70, 132415.
Yang, H. and Prewitt, C.T. (2000) Chain and layer silicates at high temperatures and pressures. In R.M. Hazen and R.T. Downs, Ed., High-Temperature and High-Pressure Crystal Chemistry, 41, 211 p. Reviews in Mineralogy and Geochemistry, Mineralogical Society of America and Geochemical Society, Chantilly, Virginia.
Zhang, L., Ahsbahs, H., Hafner, S.S., and Kutoglu, A. (1997) Single-crystal compression and crystal-structure of clinopyroxene up to 10 GPa. American Mineralogist, 82, 245–258.

MANUSCRIPT RECEIVED APRIL 3, 2008
MANUSCRIPT ACCEPTED NOVEMBER 14, 2008
MANUSCRIPT HANDLED BY GUOYIN SHEN